Transfer-free graphene synthesis by nickel catalyst dewetting using rapid thermal annealing

Yannick Bleu, Florent Bourquard, Jean- Yves Michalon, Yaya Lefkir, Stéphanie Reynaud, Anne-Sophie Loir, Vincent Barnier, Florence Garrelie, Christophe Donnet

Version of Record: https://www.sciencedirect.com/science/article/pii/S0169433221005687
Manuscript_c67ebf13da6559a4891855ed8011c2df

Transfer-Free Graphene Synthesis by Nickel Catalyst Dewetting Using Rapid Thermal Annealing

Yannick Bleu[1], Florent Bourquard[1], Jean-Yves Michalon[1], Y. Lefkir[1], S. Reynaud[1], Anne-Sophie Loir[1], Vincent Barnier[2], Florence Garrelie[1], and Christophe Donnet[1]

(1) *Université de Lyon, Université Jean Monnet-Saint-Etienne, CNRS, Institut d'Optique Graduate School, Laboratoire Hubert Curien UMR 5516, F-42023, SAINT-ETIENNE, France*
(2) *Université de Lyon, Mines Saint-Etienne, CNRS, Laboratoire Georges Friedel UMR 5307 CNRS, F-42023 Saint-Etienne, France*

Abstract

We report the transformation of amorphous carbon deposited by pulsed laser deposition (PLD) into free transfer graphene, associated with dewetting of the nickel catalyst film during rapid thermal annealing. Prior to graphene synthesis, dewetting of the pure nickel film is investigated versus thickness and temperature. Then a parametric study of graphene synthesis from an amorphous carbon film 2 nm thick is carried out by varying the starting thickness of the nickel catalyst (25, 50, 150 nm) at a temperature of 900°C. The graphene layers form on the top surface of the nickel film and at the interface between the nickel film and the SiO_2 substrate, due to rapid diffusion of C through the Ni film. The concomitant nickel dewetting process enables exposure of the interfacial graphene while some graphene layers agglomerate on nickel particles. By removing the nickel particles with an acid treatment, interfacial graphene (also called free transfer graphene) was formed directly on the SiO_2 substrate, avoiding a time consuming and relatively complicated transfer process. This work paves the way for the control of the number of layers of free transfer graphene using a solid carbon source and a nickel film catalyst.

1. Introduction

Research on graphene has received a lot of interest in recent years due to its outstanding physical and chemical properties, and its potential use in various applications**[1–5]**. For this reason, a variety of graphene synthesis techniques have been developed including mechanical exfoliation, annealing of SiC under ultrahigh vacuum, chemical vapor deposition (CVD), reduction of graphene oxide, and physical vapor deposition (PVD)**[6–9]**. Among PVD, pulsed laser deposition (PLD) is one of the alternative routes to CVD, the latter being the most commonly used process. As highlighted in our recent review paper related to the synthesis of graphene by PLD **[10]**, one of the main advantages of this process is that it allows precise

control of the thickness and composition of the carbon-based film (including the incorporated dopants) which acts as the solid-state precursor of the graphene layers. Several catalysts including nickel, copper, cobalt, copper-nickel alloy catalyst **[11–16]** have been suggested to convert the amorphous carbon film into graphene layers. Several studies have been published on the growth of graphene by PLD using a nickel catalyst **[10,17–25]**. Schematically, thermal heating induces a dissolution of carbon atoms which diffuse into the metallic catalyst. During the thermal treatment and cooling process, the carbon solubility decreases and carbon segregates as graphene layers onto the surface of the nickel catalyst. Note that such a mechanism is observed whatever the carbon film is initially localized at the interface of the substrate with the catalyst, or on the top surface of the catalyst. The control of both the homogeneity and the number of graphene layers depends strongly on the solubility and diffusion of carbon and is consequently influenced by heating parameters (heating ramp, temperature and time of heating, cooling ramp) and material parameters (mainly the thicknesses of the carbon film and nickel film). However, the influence of the thickness of the nickel catalyst film on the synthesized graphene has rarely been investigated.

By combining PLD and rapid thermal annealing, transfer-free graphene can be obtained by dewetting the nickel film. By increasing the temperature in a vacuum, dewetting is a spontaneous phenomenon in which a thin film is treated under conditions that allow the system to minimize its interfacial energy by breaking the film up into separate particles or islands. Dewetting of nickel thin films during graphene synthesis has been observed under different conditions **[26–28]**. Moreover, when an acidic treatment $FeCl_3$ or HCl solution is used, the nickel particles resulting from the dewetting process can be eliminated. This process avoids the need for relatively complicated transfer protocols in which cracks, wrinkles, and contamination of the resulting graphene can occur **[29,30]**.

In the present work, in the first step, we conducted a detailed parametric study of the influence of the thickness of the nickel and of the annealing temperature on the dewetting of nickel thin film. The morphological analysis was carried out with SEM to observe the effect of these two parameters. In the second step, we investigated the impact of the starting thickness of the nickel catalyst on the synthesized graphene by rapid thermal annealing of the a-C/Ni stacking. The samples were analyzed using SEM-EDS, Raman, UV-Vis, and HRTEM. This study advances our understanding of the influence of the starting thickness of the nickel catalyst on its dewetting process and on the resulting synthesized graphene. Indeed, the effect of the metal catalyst thickness and annealing temperature on the nanoarchitecture of the graphene film are rarely systematically investigated in the literature. From a parametric study based on various

nickel film thicknesses (25-150 nm) annealed in the temperature range 500-900°C, we demonstrate the optimized experimental conditions to obtain a dominant graphene bilayer by annealing at 900°C an amorphous carbon films 2 nm thick deposited onto a Ni film catalyst 50 nm thick. In such conditions, the results show that an easy acidic treatment is able to remove the residual nickel catalyst compatible with the existence of the graphene film onto the silica substrate.

2. Experimental details

Figure 1 shows the different steps used to prepare the sample. SiO_2 substrates were ultrasonically cleaned, first in acetone, and then in ethanol, and finally in deionized water baths. Nickel film (25, 50, 150 nm thick) was deposited by thermal evaporation on top of the cleaned SiO_2 substrates in a vacuum chamber pumped to a base pressure of 10^{-6} mbar. High purity Ni (99.99%) was molten thermally in a tungsten nacelle and evaporated towards the substrate.

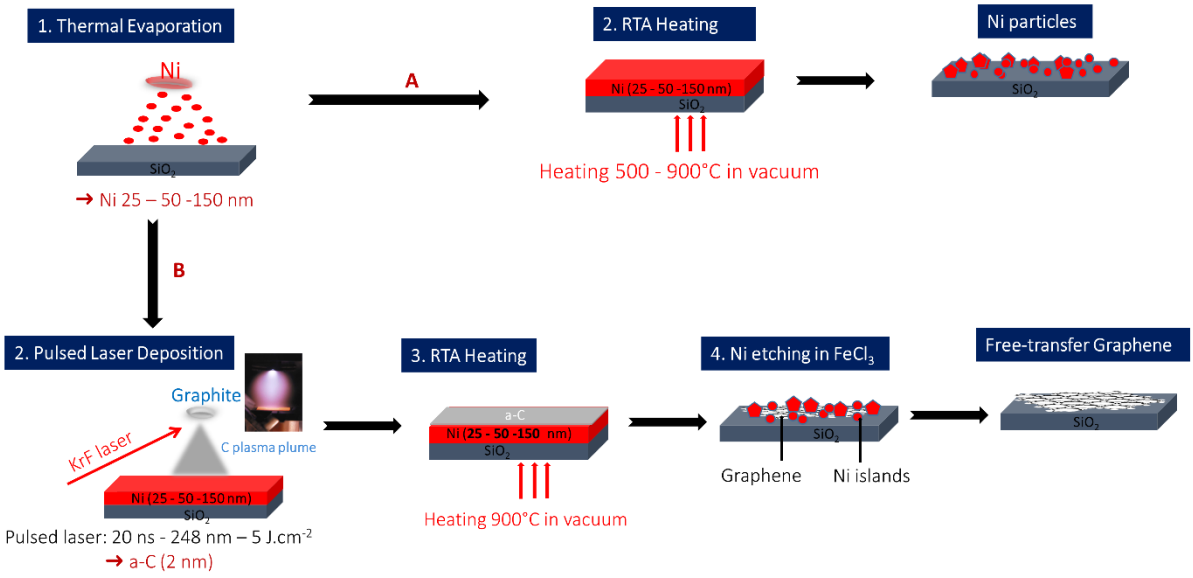

Figure 1: Synthesis route for (A) rapid thermal annealing of Ni thin films and (B) free-transfer graphene films obtained by pulsed laser deposition of carbon on Ni thin films followed by rapid thermal annealing and Ni etching. In both cases, the substrate was SiO_2. Inspired from **[31]**, with permission.

Thermal annealing of nickel thin film (labeled A in Fig. 1): After deposition of the nickel thin film (25, 50, 150 nm thick) by thermal evaporation, the Ni/SiO_2 samples were annealed using rapid thermal annealing (RTA) to study nickel dewetting. Annealing was performed in a RTA oven at 500, 700, 800, and 900 °C for 420 s in a vacuum pressure of 10^{-2} mbar, with a heating rate of +15 °C/s and a cooling rate of about -0.5 °C/s. An annealing time of 420 s was chosen for all temperatures based on our previous investigation of the graphene growth

mechanism studied using in situ XPS **[25]**, which showed that phase equilibrium was reached at 500 °C with 150 nm of Ni when heated for similar periods of time. In the present study, we thus assumed that phase equilibrium is also reached after heating for 420 s at temperatures ranging from 500-900 °C, with Ni film thicknesses ranging from the 25-150 nm.

Free transfer graphene synthesis process (labeled B in Fig. 1): Ni/SiO_2 substrates were introduced in a vacuum PLD chamber pumped to a base pressure of 10^{-7} mbar for 2 nm of amorphous carbon (a-C) deposition. Carbon was ablated from a high purity graphite (99.9995%) target using an excimer KrF laser (248 nm wavelength, 20 ns pulse duration, 10 Hz repetition rate) at room temperature. The fluence of the laser beam was kept constant at 5 $J.cm^{-2}$. The distance between the sample holder and the graphite target was 40 mm. The final step consisted of annealing the $a\text{-}C/Ni/SiO_2$ samples at 900 °C for the transformation of amorphous carbon into graphene. The choice of a-C film thickness (2 nm) and annealing conditions (temperature of 900°C, heating and cooling ramps) is based on our previous graphene synthesis optimization from a wide set of synthesis conditions **[31]**. The sample was heated for 420 s at a vacuum pressure of 10^{-2} mbar in an RTA oven, with a heating rate of +15 °C/s and a cooling rate of about -0.5°C/s. After graphene growth, the samples were immersed in 4M $FeCl_3$ for 24 h to remove nickel particles. **Table 1** summarizes the processing conditions of the samples.

<table>
<tr><th>Samples</th><th>Thickness of nickel thin film</th><th>Annealing temperature</th><th>Heating rate
Annealing time
Cooling rate</th></tr>
<tr><td>As deposited</td><td rowspan="6">25 nm

50 nm

150 nm</td><td>-</td><td rowspan="6">+ 15 °C/s

420 s

- 0.5°C/s</td></tr>
<tr><td>Ni-500</td><td>500 °C</td></tr>
<tr><td>Ni-700</td><td>700 °C</td></tr>
<tr><td>Ni - 800</td><td>800 °C</td></tr>
<tr><td>Ni - 900</td><td rowspan="2">900 °C</td></tr>
<tr><td>a-C (2nm) / Ni – 900</td></tr>
</table>

Table 1: Summary of growth conditions.

Graphene was characterized by Raman spectroscopy using an Aramis Jobin Yvon spectrometer (Horiba Jobin Yvon, Gières, France), with 442 nm (2.81 eV) excitation laser-focused through an ×100 objective with a high aperture, guaranteeing the micrometric resolution of the analysis, and providing precise Raman mapping of the samples. To analyze the uniformity of the synthesized graphene, mapping of the samples over probed surfaces 20 × 20 micrometers in size, was performed with graphene at 442 nm, totaling 400 Raman spectra per map with a 1 μm spot size collected for each sample. Scanning electron microscopy (SEM) coupled with EDS was performed using a FEI Novanano SEM 200 operated at 15kV. The statistical values were extracted from the SEM images using ImageJ software. UV–Visible spectroscopy in transmission mode was performed by a spectrophotometer Cary50 Probe (Varian) within the spectral range 200–800 nm. High-resolution transmission microscopy (HRTEM) was performed using a JEOL NEOARM microscope, equipped with a spherical aberration corrector, operating at an acceleration voltage of 60 kV and an emission current of 10 μA. Free transfer graphene sheets were collected on a holey carbon copper grid. The spatial resolution was < 0.1 nm.

3. Results

3.1. Effect of rapid thermal annealing on the morphology of nickel thin film

Fig. 2a, f, and k show that the nickel thin film completely and uniformly covered the SiO_2 substrate before the thermal annealing process started. With annealing at increasing temperatures, a reduction in the extent of the surface covered by nickel was observed. This was due to a dewetting process of the nickel film on the SiO_2 surface, as already observed with various metallic thin films annealed in vacuum conditions **[32–36]**. The dewetting process of continuous metal films generally takes place in three successive stages:

1) holes form inside the Ni film due to the beginning of surface Ni diffusion (stage 1),
2) the density of holes increases with the transition from the continuous Ni film to an almost continuous surface network of stringy Ni (stage 2),
3) the final transition occurs from the stringy Ni network to a surface distribution of individual Ni (sub-) micrometer-sized particles (stage 3).

This thermally induced process leads to the gradual formation of nickel particles on the SiO_2 substrate, due to minimization of the total surface energy of the system.

Fig. 2 shows SEM images of the surface of the annealed nickel thin film of varying thickness (25, 50 and 150 nm) on top of the fused silica SiO_2 substrates after annealing at 500 °C ((b) (g) and (l)), 700 °C ((c), (h) and (m)), 800 °C ((d), (i) and (n)), 900 °C ((e), (j) and (o)). The first line corresponds to the images of changes in the 25 nm thick nickel thin film during dewetting; the second line corresponds to the 50 nm thick film and the third line to the 150 nm thick nickel thin film. The first column in **Fig. 2** shows that the nickel thin films as deposited on SiO_2 samples are quite homogeneous with low roughness, regardless of their thickness. The second column corresponds to the SEM images of the annealed samples at 500 °C for the three different nickel film thicknesses. From 500 °C upward, the transition between the three above-mentioned stages can be observed, but at different temperatures depending on the starting thickness of the Ni film, as depicted in **Fig. 2** and described below.

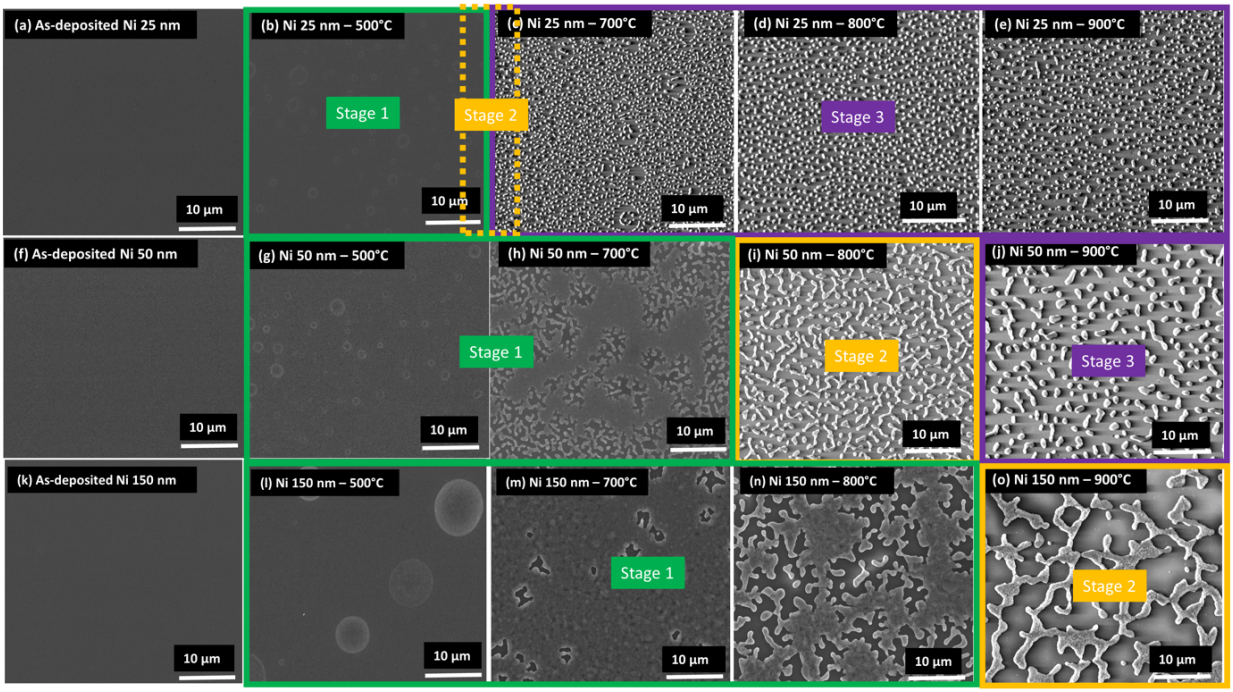

Figure 2: Summary of the solid-state dewetting behavior of nickel thin films deposited on a fused silica SiO_2 substrate: SEM images of the dewetting of 25 nm thick nickel thin film (a-e), 50 nm thick (f-j) and 150 nm thick (k-o), as a function of annealing temperature (range 500-900 °C). The three stages related to the Ni dewetting mechanism, described in the text, are superimposed on the SEM images.

Stage 1, corresponding to the formation of spherical holes was observed at 500 °C, with different hole sizes and densities depending on the thickness of the Ni film. Stages 2 and 3 were clearly observed in 50 nm thick Ni within the 700-900 °C range. At 800 °C (**Fig. 2i**), the end of stage 2 was visible with an almost-continuous surface network of stringy Ni being transformed into individual Ni particles corresponding to the beginning of stage 3. At 800 °C,

the stringy Ni particles were less separated than at 900 °C (**Fig. 2j**) clearly corresponding to stage 3 with a surface distribution of individual Ni (sub-) micrometer-sized particles.

On the one hand, when the Ni film was thin (25 nm), stage 3 occurred when the temperature was as low as 700 °C (**Fig. 2c**), and higher temperatures only led to a slight increase in the size of the individual Ni particles. On the other hand, when the Ni film was thicker (150 nm), stage 2 was observed at higher temperatures compared to thinner Ni films, as shown in **Fig. 2o** related to an annealing temperature of 900°C, with an almost continuous surface network of stringy Ni islands that were significantly bigger than with the 50 nm thick Ni at 800 °C (**Fig. 2i**). No stage 3 was observed in the 150 nm thick Ni. Higher temperatures are probably required to form individual Ni particles. We clearly observed that the three-stage dewetting process depended on the starting thickness of the nickel film and on the annealing temperature. We also observed that dewetting accelerated with increasing thinness of the film, and that the temperature at which dewetting occurred decreased with increasing film thinness, in agreement with Thompson **[32]**. In this fundamental article related to solid-state dewetting of thin film, Thompson detailed the mechanism responsible for the dewetting of metastable as-deposited thin films at temperatures well below the film's melting temperature, by the minimization of the total energy of the free surfaces of the film and substrate, and of the film-substrate interface. A decrease of the film thickness generally induces a decrease of the temperature at which dewetting occurs, due to an increase of the driving force for dewetting and thus an acceleration of the dewetting rate. Preexisting holes, film edges or formation of new holes are mandatory for the dewetting process. As observed in our stage 1, the temperature of hole formation and growth decreases as the Ni film thickness is lower. Then the holes grow to form dewetted areas and often overlap (in agreement with our stage 2), to form a complete dewetted film (in agreement with our stage 3). Thompson noticed that the dewetting temperature decreases with the initial film thickness, and the dewetting-induced islands size and spacing also decrease by the same way. This is also confirmed by Geissler et al. **[37]** in an experimental configuration close to ours. This could explain why the 25 nm thick Ni film started to coalesce at a lower temperature than the thicker Ni films, and why the thickest film (150 nm) started to coalesce into nickel islands at the highest temperatures. In other words, the transition between the three above-mentioned stages occurred at higher temperatures with increasing thickness of the Ni film.

Using ImageJ software, the SEM images in **Fig. 2** were used to extract information concerning surface coverage by the Ni islands or particles, the perimeter of the particles, and interparticle spacing (i.e. the distance to the nearest neighbor particles), as seen in **Table 2**.

Samples	Processing temperature (°C)	Average perimeter (µm)	Surface coverage (%)	Particles interspacing (µm)
Ni 25 nm	700	1.47 ± 0.5	21	0.62
	800	1.88 ± 0.5	19	0.80
	900	1.70 ± 0.8	16	0.84
Ni 25 nm with Graphene	900	1.04 ± 0.6	11	0.70
Ni 50 nm	800	N/A	24	N/A
	900	3.90 ± 2.3	16	1.50
Ni 50 nm with Graphene	900	2.34 ± 1.18	15	1.10
Ni 150 nm	800	N/A	58	N/A
	900	N/A	35	N/A
Ni 150 nm with Graphene	900	N/A	14	N/A

Table 2: Summary of the statistical values of the average perimeter, surface coverage, and interspacing of nickel particles extracted from the SEM images in **Fig. 2**, **5a**, **7a** et **8a**.

Whatever the thickness of the film, the surface coverage by the stringy Ni islands (stage 2) or particles (stage 3) decreased, from 21% to 16% in the 25 nm thick film, from 24% to 16% in the 50 nm thick film, and from 58% to 35% in the 150 nm thick film, all with an increase in temperature. This is consistent with the dewetting and coalescence mechanism described above. Moreover, at the highest temperature of 900 °C, the thicker the original Ni film (150 nm), the higher the surface coverage. The particle perimeter and interparticle distance could only be extracted and compared in stage 3, i.e. with the 25 nm thick film annealed at 700, 800, and 900 °C, and with the 50 nm thick film annealed at 900 °C. **Fig. 3** shows the size distribution of the perimeter of the Ni particles associated with the dewetting process of 25 nm thick nickel film. The average particle perimeters were 1.47 ± 0.5, 1.88 ± 0.5 and 1.70 ± 0.8 µm, and the interparticle spacing was 0.62, 0.80, 0.84 µm, at annealing temperatures of 700, 800, 900 °C, respectively. At the highest temperature of 900 °C, the perimeter of the particles related to the thicker 50 nm film was slightly more than double compared to the 25 nm thick film (3.9 µm vs 1.7 µm) at the same temperature, and the interparticle spacing was a little less than double (1.50 µm compared to 0.84 µm), with a similar surface coverage of 16%. Thus, at a given temperature, we observed a significant dependence of particle size and distribution with the initial nickel film thickness. These results are in good agreement with previously reported

results on the high-temperature dewetting of metal thin films, including Ni **[37,38]**, observed in similar thermo-kinetic experimental heating conditions. Finally, we cannot exclude the possibility that residual Ni was still present in the Ni particles, implying that Ni dewetting was not complete, even at 900 °C. This hypothesis is examined in the following section related to the behavior of the Ni film at the highest temperature (900 °C) using a carbon film to achieve graphene synthesis.

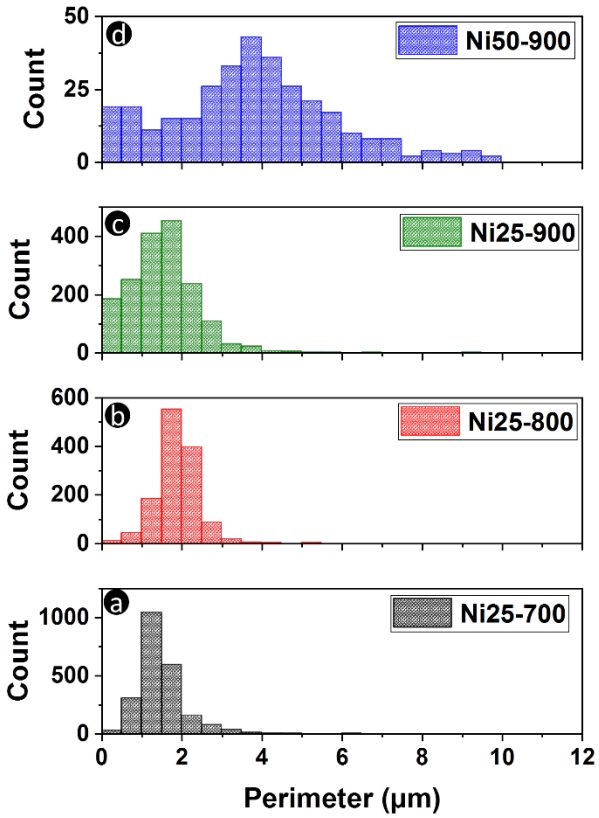

Figure 3: Particle size distribution corresponding to the 3rd stage of the Ni dewetting process, obtained using ImageJ software on the SEM images in Fig.2, and related to the 25 nm thick Ni film after thermal annealing at 700 °C (a), 800 °C (b) and 900 °C (c), and the 50 nm thick Ni film after thermal annealing at 900 °C (d).

3.2. Influence of nickel thickness on the transformation of amorphous carbon into graphene after thermal annealing at 900 °C

At the highest RTA temperature of 900°C and 10^{-2} mbar pressure used in our study, the nickel was still well below its melting point (1455 °C). It therefore remained in solid-state, but was progressively dewetted, as evidenced in the previous section, via the three-stage mechanism

with varying temperature thresholds depending on the starting thickness (25, 50, 150 nm) of the Ni film. However, data in the literature on graphene synthesis using a solid carbon film in the presence of a Ni catalyst, indicate that carbon dissolves into Ni in a temperature range corresponding to the dewetting process of the Ni film, before its surface segregation into graphene layers **[25,39]**. The objective of this section is thus to elucidate how nickel dewetting remains compatible with the synthesis of graphene and to assess the quality of graphene obtained in such conditions. Ideally, such a process would avoid having to transfer the graphene onto another substrate, if the residual Ni particles could be removed from the surface, for example with an acidic treatment. This section is thus focused on the formation of graphene from a very thin carbon film (2 nm), deposited on the 25, 50, and 150 nm thick Ni film, after RTA at 900 °C. We selected the highest temperature studied in the previous section to investigate graphene formation coupled with the most advanced stage of Ni dewetting, considering the annealing temperature range available in our set of experiments.

a. Graphene growth using a 25 nm thick nickel thin film catalyst

Fig. 4 shows the results of Raman analysis of the synthesized graphene using the 25 nm thick nickel catalyst film, after thermal annealing at 900 °C. The most significant peaks for graphene films revealed by Raman spectroscopy are D, G, and 2D, located around 1,350, 1,580, and 2,700 cm^{-1} respectively. In addition, their intensity ratio can be used to estimate the presence of defects (I_D/I_G) and the number of graphene layers (I_{2D}/I_G). To distinguish between monolayer, bilayer and few-layer graphene, we considered that an I_{2D}/I_G ratio >1.4 is associated with the formation of monolayer graphene, an I_{2D}/I_G ratio located between 0.75 and 1.4 is associated with a bilayer graphene, and an I_{2D}/I_G ratio < 0.75 is associated with few-layer graphene (3 or more layers). These considerations are reported in **[40–45]**. Due to the penetration depth of the Raman probe, it is worth noting that all these maps include the graphene on the surface of the nickel particles as well as the graphene at the interface between the nickel nodules and the SiO_2 substrate.

Fig. 4a shows the Raman mapping of the I_D/I_G ratio, where the average value is 0.25 with a very low standard deviation of 0.05, suggesting the good uniformity of the synthesized graphene with low defect density. **Fig. 4b** shows the Raman mapping of the I_{2D}/I_G ratio with a mean value of 0.62 and a low standard deviation of 0.05. This result demonstrates the formation of a uniform few-layer (3-6 layers) graphene using a 25 nm thick nickel film catalyst. **Fig. 4c** shows a representative spectrum extracted from Raman mapping. In this spectrum, the D, G, and 2D peaks are located at 1,372, 1,587, 2,746 cm^{-1}, respectively. The intensity ratios are 0.21

for I_D/I_G and 0.67 for I_{2D}/I_G. The average crystallite size L_a is 44 nm. This value is derived from the I_D/I_G ratio by the mean of the Tuinstra–Koenig equation**[46]**.

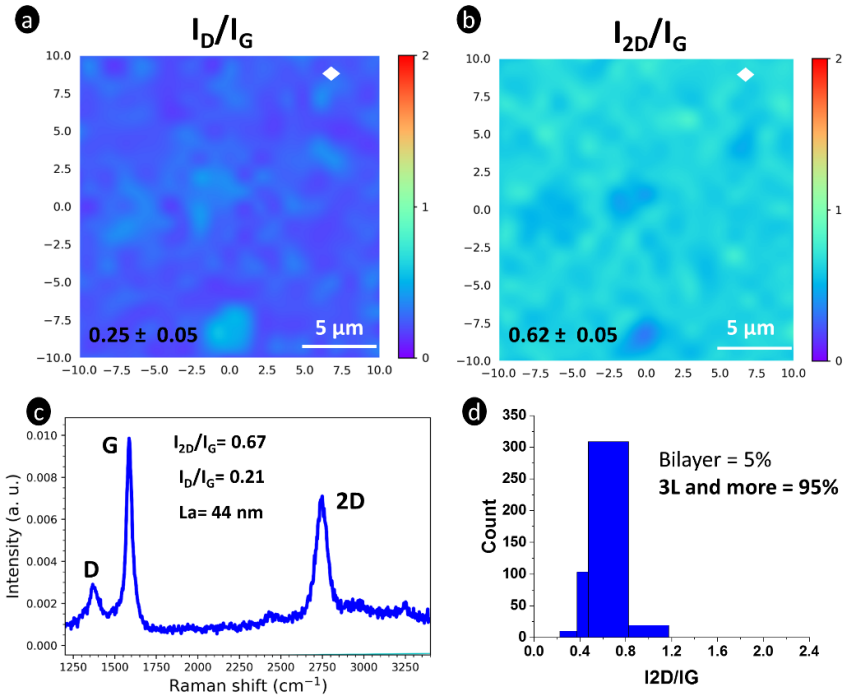

Figure 4: Raman analysis of the synthesized graphene using a 25 nm thick nickel catalyst: (a) Raman mapping of the I_D/I_G ratio in a 20 ×20 µm² region with the average value of 0.25; (b) Raman mapping of the I_{2D}/I_G ratio in a 20 ×20 µm² region with the average value of 0.62; (c) A representative spectrum extracted from the mapping of the synthesized graphene: its position is shown by the white diamonds on the Raman maps; (d) Statistical histogram of the Raman mapping of I_{2D}/I_G ratio showing the predominance of few-layer graphene.

Fig. 4d illustrates the predominance of few-layer (3-6 layers) graphene with the statistical histogram of the Raman mapping of the I_{2D}/I_G ratio showing the distribution of the number of graphene layers. Indeed, with the 25 nm thick Ni film, only 5% of the mapped area is a bilayer, whereas three or more graphene layers cover 95% of the area. This suggests that the synthesized graphene is uniform even with the presence of the nickel particles derived from the dewetting of the nickel catalyst film. **Fig. 5a** shows the SEM image of the as-grown graphene using the 25 nm thick nickel film catalyst after thermal annealing at 900 °C. A similar nickel island distribution as that obtained with the 25 nm thick Ni film annealed at the same temperature (**Fig. 2e**) is observed. By comparing the statistical values of the pure Ni film (**Fig. 3a**) with the same film covered by graphene, the perimeter of the nickel particles is reduced from 1.70 µm without graphene to 1.04 µm with graphene. The surface coverage decreased from 16 to 11% and the average distance between the particles decreased slightly from 0.80 to 0.70 µm. This

difference may be due to the presence of dissolved carbon in the nickel, which modifies the surface energy of the nickel during the dewetting process, as discussed in the Discussion section.

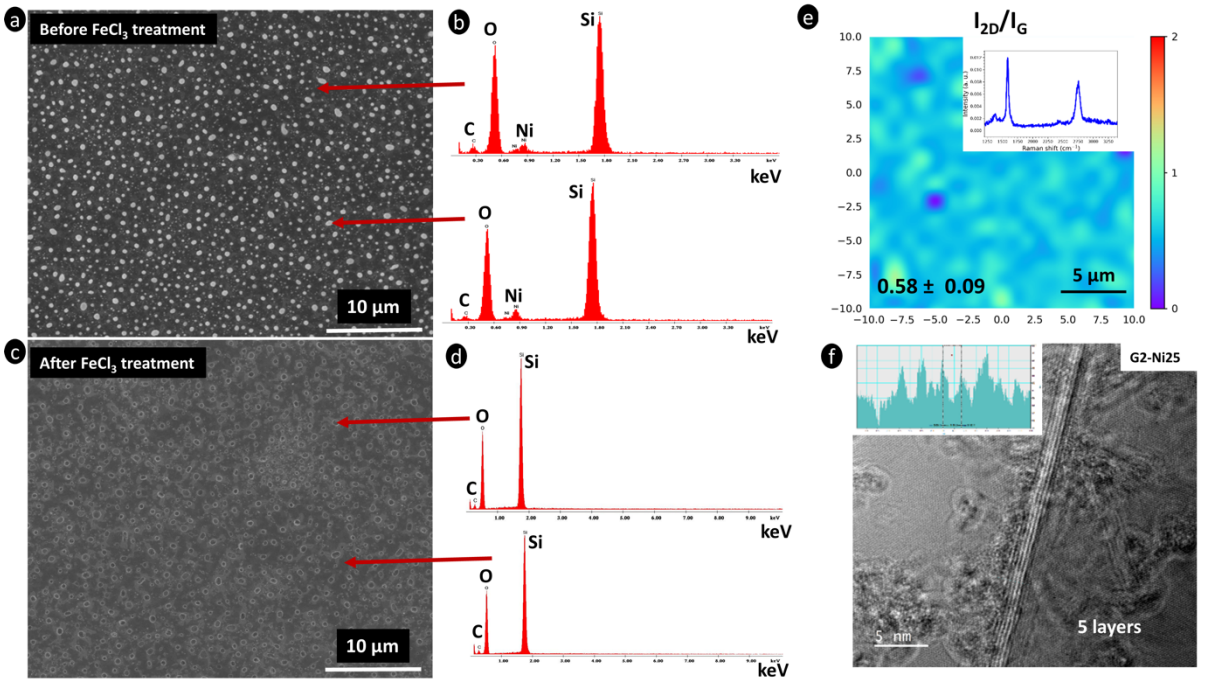

Figure 5: (a) SEM image of the as-synthesized graphene using 25 nm thick nickel catalyst, after annealing at 900 °C; (b) EDS spectra of two different regions of the samples, the grey-black zone (at the top) and the white zone (below); (c) SEM image of the graphene treated with $FeCl_3$ to remove the nickel particles leading to the appearance of the interfacial graphene; (d) EDS spectra of two different regions of the samples, the zone with traces of islands (at the top) and the grey-black zone (below), both showing the absence of nickel; (e) Raman mapping of the I_{2D}/I_G ratio in a 20 ×20 µm² region with an average value of 0.58 of the interfacial graphene after $FeCl_3$ treatment. The inset shows a representative spectrum extracted from Raman mapping; (f) HRTEM image of the graphene edges after $FeCl_3$ treatment showing five layers. The inset is the intensity profile image.

Fig. 5c shows SEM image of the graphene treated with $FeCl_3$ acidic solution; this graphene can be called interfacial graphene because the other graphene on the surface of the nickel nodules probably disappeared with the removal of residual nickel. Spherical white traces left by the disappearance of the nickel nodules are visible. **Fig.5 b, d** show EDS spectra, with atomic concentrations depicted in **Table 3**, for the as-grown graphene and the $FeCl_3$ treated graphene. For the as-grown graphene (**Fig. 5b**), the spectra were captured by focusing the electron-beam spot either on the nickel particle (lower spectrum), or on the graphene layer (upper spectrum). The results revealed that these two areas contain nickel and other expected elements such as C,

O, and Si. However, the area corresponding to the Ni particles contains a bit more nickel than the other region. This means that the dewetting of Ni on the original surface was not complete, even at 900 °C. However, after $FeCl_3$ treatment, the EDS spectra recorded both inside and outside the footprints left by the removed nickel particles (**Fig. 5d** and **Table 3**) showed no Ni signals. This result is consistent with previously reported studies**[27,28]** on acidic etching to obtain transfer-free graphene.

	Before $FeCl_3$				After $FeCl_3$			
	C (at.%)	O (at.%)	Ni (at.%)	Si (at.%)	C (at.%)	O (at.%)	Ni (at.%)	Si (at.%)
G-Ni-25 nm	17.0	52.0	3.5	27.5	18.0	53.5	0	28.5
G-Ni-50 nm	10.5	61.5	3.5	24.5	12.0	60.0	0	28.0
G-Ni-150 nm	5.5	64.0	8.0	22.5	-	-	-	-

Table 3: Quantitative EDS analysis, before and after $FeCl_3$ treatment, of the graphene surface synthetized using the 25, 50 and 100 nm thick nickel catalyst films, after thermal annealing at 900 °C.

Fig. 5e shows the Raman mapping of the I_{2D}/I_G ratio in a 20 ×20 μm² region associated with interfacial graphene after treatment with $FeCl_3$, with an average value of 0.58. The inset shows a representative spectrum extracted from the Raman mapping. Both exhibit the same characteristics as the spectrum for as-synthesized graphene shown in **Fig. 4b-c**. The surface graphene distribution is uniform, like the as-grown graphene. However, we observed a decrease of the I_D/I_G ratio, from 0.25 ± 0.05 before the acidic treatment to 0.19 ± 0.12 after the acidic treatment, consistent with a decrease of the defective level and/or increase of size of the graphitic clusters in the graphene layers. This suggests that the $FeCl_3$ treatment is a transfer-free process that allows the removal of the Ni catalyst with no significant alteration of the dominant few-layer architecture, but with some modifications on the defective level of the graphene films. From our best of knowledge, this last observation has never been reported nor discussed previously in the literature. Its interpretation requires more specific attention in the future. **Fig. 5f** shows the HRTEM images of the graphene after $FeCl_3$ treatment. The images, typical of graphene edges, is an accurate way to measure the number of graphene layers at different locations. Here, the synthetized graphene from 25 nm thick Ni displays five lines representing the five layers graphene (**Fig. 5f**) revealed by Raman analysis.

b. Graphene growth using 50 nm thick nickel thin film catalyst

Like for the synthesized graphene using 25 nm thick nickel film, Raman analysis and SEM-EDS were performed for the as-grown graphene on the 50 nm thick nickel after thermal annealing at 900 °C. Again, all the maps include the graphene on the surface of the nickel

particles as well as the graphene at the interface between the nickel nodules and the SiO_2 substrate.

Fig. 6a shows the Raman mapping of the I_D/I_G ratio, where the average value is 0.26 with a low standard deviation of 0.13, suggesting the density of defects in the synthesized graphene is reasonably uniform. **Fig. 6b** shows the Raman mapping of the I_{2D}/I_G ratio with a mean value of 1.08 and a high standard deviation of 0.38. This result demonstrates the formation of continuous, but non-uniform graphene using 50 nm thick nickel catalyst. The graphene derived from the 50 nm thick nickel is indeed heterogeneous, containing monolayer, bilayer, and few-layer graphene. This observation was confirmed by the statistical histogram of the Raman mapping of the I_{2D}/I_G ratio showing the distribution of the number of graphene layers in **Fig. 6c**. From these statistical data, 7% of the mapped area were few-layer (3 and more layers), 70% were bilayer and 23% were monolayer, suggesting the bilayer predominance in the mapped area. **Fig. 6d** shows the different types of Raman spectra representative of monolayer, bilayer, and few-layer graphene with their characteristic values. This is the same finding as that reported in our previous study **[31]** confirming our method is reproducible.

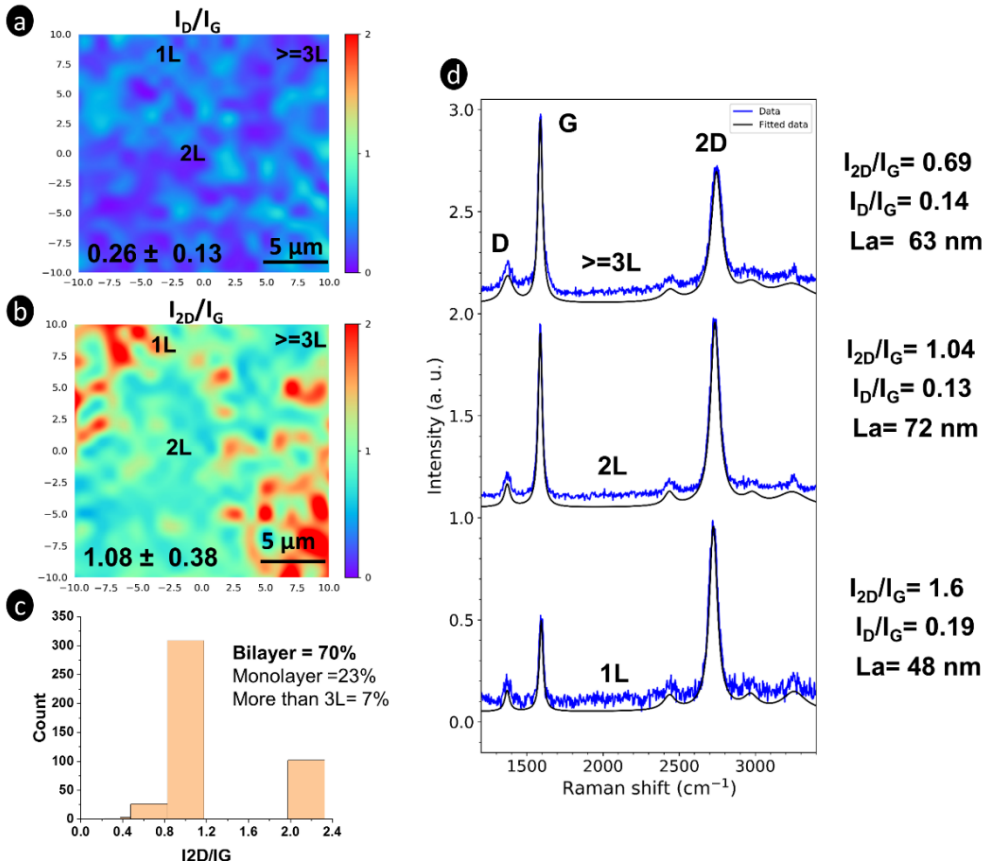

Figure 6: Raman analysis of the as-synthesized graphene using 50 nm thick nickel catalyst film: (a) Raman mapping of the I_D/I_G ratio in a 20 ×20 µm² region with the average value of 0.26; (b) Raman

mapping of the I_{2D}/I_G ratio in a 20 ×20 μm² region with the average value of 1.08; (c) Statistical histogram of Raman mapping of the I_{2D}/I_G ratio showing that bilayer graphene predominates. (d) Representative spectra from the mapping of the as-grown graphene, their positions are highlighted with the corresponding number of the layer in the Raman mappings.

Fig. 7a shows the SEM image of the as-grown graphene using 50 nm thick nickel catalyst. Like the annealed 50 nm thick nickel, this sample displays many island-shaped nickel particles. Comparison of the statistical values showed that the perimeter of nickel particle decreased from 3.9 μm with no graphene to 2.34 μm with graphene. The surface coverage decreased slightly from 16 to 15% and the average distance between the particles from 1.50 to 1.10 μm. This is the same trend as that observed using 25 nm thick nickel film. The SEM image (**Fig. 7c)** of the graphene treated with $FeCl_3$ shows that the round-shaped nickel particles are no longer present. Elemental analysis with EDS was performed of the as-grown graphene and of the treated graphene. The results showed the presence of nickel in the as-synthesized graphene sample (**Fig. 7b** and **Table 3**), while the removal of nickel was confirmed in the treated graphene spectrum (**Fig. 7d** and **Table 3**). **Fig. 7e** shows the Raman mapping of the I_{2D}/I_G ratio in a 20 ×20 μm² region with an average value of 0.91, associated with the graphene treated with $FeCl_3$ leading to the interfacial graphene. The inset spectrum shows the one of bilayer graphene. As for the 25 nm thick film, we also observed a decrease of the I_D/I_G ratio, from 0.26 ± 0.13 before the acidic treatment to 0.15 ± 0.10 after the acidic treatment, consistent with an effect of the acidic treatment on the defective level and/or size of the graphitic clusters in the graphene layers, which remains not explained at the present stage of investigation. This mapping shows that the interfacial graphene has the same characteristics as the as-grown graphene, except the defective level, meaning the interfacial graphene is also continuous but non-uniform, as it contains monolayer, (mainly) bilayer, and some few-layer graphene. **Fig. 7f** shows the HRTEM images of the edges in the bilayer graphene region displaying a double line. The interplanar spacing estimated from the intensity profile images was 0.345 nm, as shown in the insets of **Figs. 5f** and **7f**. Such a value is in agreement with previously reported works **[47,48]**. **Fig. 7g** shows a typical graphene monolayer region indicated by the red circle, and **Fig. 7h** shows the hexagonal structure of this typical monolayer illustrated with the purple dots. The HRTEM examination again confirms that the starting thickness of the nickel strongly affects the final synthesized graphene layers, thereby confirming our Raman results.

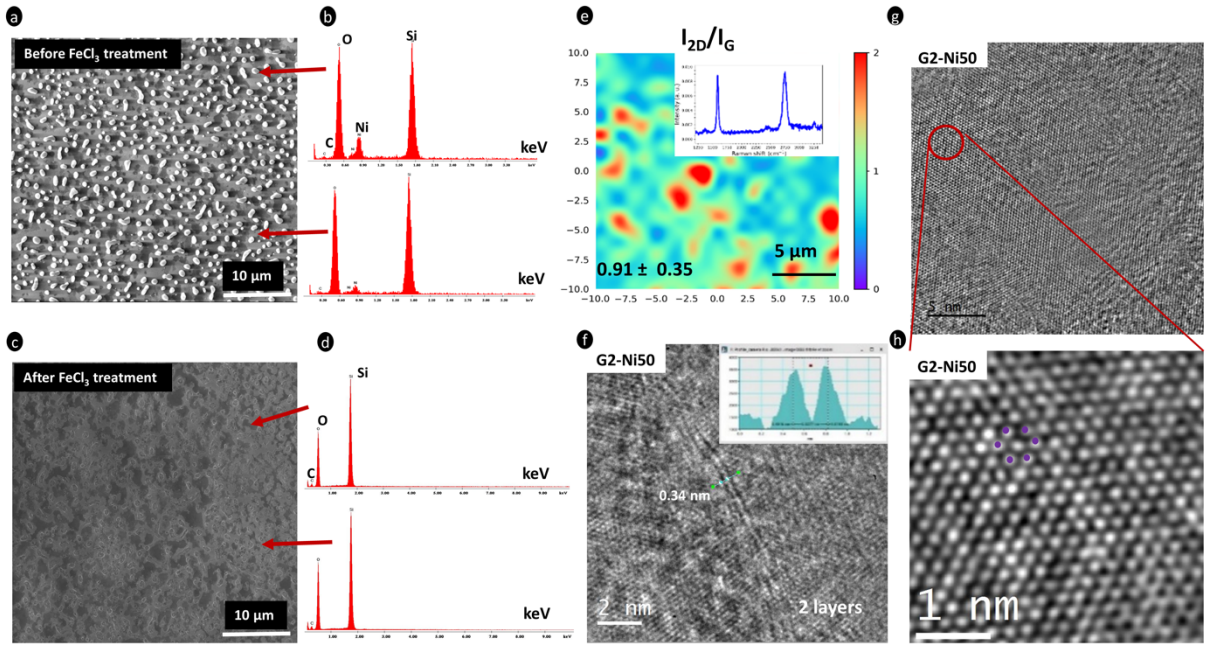

Figure 7: (a) SEM image of the as-synthesized graphene using the 50 nm thick nickel catalyst film. (b) EDS spectra of two different regions of the samples, the zone with the white islands (at the top) and the grey-black zone (below). (c) SEM image of the graphene treated with $FeCl_3$ to remove the nickel particles leading to the appearance of interfacial graphene (d) EDS spectra of two different regions of the samples, the zone with traces of islands (at the top) and the grey-black zone (below), both showing the absence of nickel. (e) Raman mapping of I_{2D}/I_G ratio in a 20 ×20 µm² region with the average value of 0.91 of the graphene treated with $FeCl_3$. The inset shows a bilayer graphene spectrum from the Raman mapping of the $Fecl_3$ treated graphene. (f) HRTEM of graphene edges resulting from the use of 50 nm thick nickel, showing two layers after $FeCl_3$ treatment. The inset is the intensity profile image. (g – h) HRTEM of resulting graphene from the use of 50 nm thick nickel, showing a "one monolayer" area (red circle) and the hexagonal atomic resolution of the monolayer graphene. The purple dots in the inset in Fig. 7h highlight the hexagonal structure of graphene.

c. Graphene growth using 150 nm thick nickel thin film catalyst

Graphene was formed using a 150 nm thick nickel film as catalyst after thermal annealing at 900 °C. Like the annealing response with 150 nm, where thick nickel differed from the response when 25 and 50 nm thick nickel was used, the resulting graphene also differed. The first striking point is that the synthesized graphene was not continuous as can be seen in **Fig. 8**. **Fig. 8a** shows the SEM image of the as-grown graphene using 150 nm thick nickel. This image has the same features as with the 150 nm thick nickel film annealed at 900 °C, with the agglomeration of

stringy nickel islands, which are less connected than in the case with no carbon. In addition, graphene formed on the surface of nickel islands and in the interface between the nickel and the SiO_2 substrate, like with 25 and 50 nm thick nickel. The difference here is the presence of graphene with a different contrast: dark contrast with more layers and bright contrast with a few layers, as reported in previous works **[49–51]**. The locations of the thin and thick graphene layers are identified by the layer numbers in the SEM image. **Fig. 8b** and **Table 3** presents the EDS analysis. Clearly the synthesized graphene is not continuous.

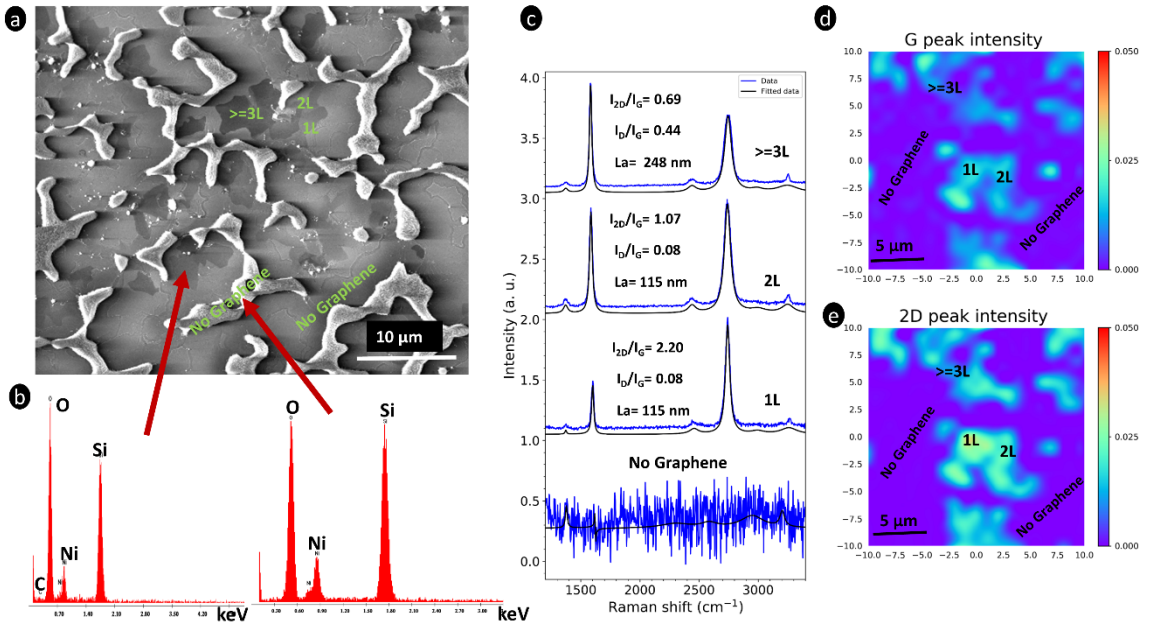

Figure 8: (a) SEM image of the as-synthesized graphene using the 150 nm thick nickel catalyst film, showing a dark and bright contrast for thicker and thinner graphene, respectively. (b) EDS spectra of two different regions of the samples, the grey-black zone (on the left) and the white islands zone (on the right). (c) Representative spectra from the sample of the as-grown graphene, their positions are identified by the number of the corresponding layer in the Raman mapping. (d) Raman mapping results of G peak intensity with a sample area of 20 ×20 µm². (e) Raman mapping results of 2D peak intensity with a sample area of 20 ×20 µm².

Fig. 8c shows the representative Raman spectra of the synthesized graphene using 150 nm thick nickel. The resulting graphene is not continuous; it contains monolayer, bilayer, and few-layer graphene like that derived from 50 nm thick nickel film. It is heterogeneous, with a very low defect density and larger crystallites than the graphene derived from 25 and 50 nm thick nickel film. The Raman spectrum of the area without graphene is presented at the bottom of **Fig. 8c**, showing no signal. This result is consistent with the synthesis graphene using nickel catalyst film with a starting thickness < 170 nm **[45]**. Raman mapping was performed to provide more arguments for the discontinuity and the non-uniformity of the synthesized graphene. **Fig. 8 d-e**

show Raman mapping of the G and 2D peak intensities, respectively, where the low-intensity areas are regions with no graphene. From all these analyses, we concluded that 150 nm thick nickel catalyst will not produce continuous graphene when 2 nm of amorphous carbon is used as a carbon source and 900 °C is used as processing temperature.

4. Discussion

4.1. Nickel thin film dewetting during rapid thermal annealing

In the results section, we demonstrated that the dewetting of nickel thin film during rapid thermal annealing leads to the formation of nickel particles. These results are crucial for the interpretation of results obtained in the presence of carbon for graphene synthesis and are discussed in the following sub-section.

The shape, size, surface coverage, and interspacing of these particles depend on the starting thickness of the film and on the annealing temperature. **Table 2** summarizes the statistical values extracted from the SEM images in **Fig. 2**, **5a**, **7a,** and **8a**.

We observed a huge effect of temperature on the shape, size, surface coverage, and interspacing of the Ni particles. Indeed, whatever the starting thickness of the nickel, the statistical parameters concerned evolved when the annealing temperature was changed. This effect shows that the formation process of the nickel particles is thermally activated, in agreement with Ostwald's ripening and atomic diffusion, these being the mechanisms generally put forward to explain the growth of particles from a thin metal film**[38,52,53]**. In fact, in Ostwald's ripening, the mass transport of individual metal atoms or clusters occurs at temperatures below the melting point of the metal. Moreover, the temperature at which dewetting occurs is lower for thinner films, and the island size scales with the film thickness**[54]**. We believe that our nickel dewetting process is due to Ostwald's ripening, as reported in previous studies on the nickel dewetting process **[37,52]**. It has been also reported **[55]** that the surface coverage decreases with an increase in the annealing temperature. Such a behavior is also observed in our study: whatever the starting thickness of the nickel film, the surface coverage decreased with an increase in temperature.

In the presence of carbon, the size, spacing, and surface coverage of the Ni islands decreased in comparison to in the absence of carbon. This suggests that carbon favors the dewetting of nickel particles, in agreement with the work of Diarra et al. **[56]**. Furthermore, the dewetting of nickel is much more pronounced with a decrease in the thickness of the original nickel film.

From all these results, we conclude that the most important aspects that affect the nickel islands derived from the dewetting of nickel thin film are the annealing temperature, the starting thickness of the nickel film, and the presence of carbon deposited prior to rapid thermal annealing.

4.2. Influence of the initial thickness of nickel thin film catalyst on graphene synthesis

In the results section, we demonstrated that the synthesized graphene resulting from the transformation of amorphous carbon using nickel catalyst is highly impacted by the starting thickness of the nickel catalyst film. **Table 4** summarizes the different characteristics of the graphene resulting from the synthesis process using 25, 50, and 150 nm thick nickel film. The results reported in **Table 4** show that increasing the nickel thickness from 25 to 50 nm reduces the number of layers in the resulting graphene. This is consistent with previously reported works **[28,57,58]**, in which the graphene films derived from thicker metal films have better structural qualities with fewer layers. Indeed, by increasing the nickel thickness from 25 to 50 nm, the graphene layer number switched from few-layer (3-6 layers) to bilayer predominance. In both cases, the derived graphene was continuous with low defect density. In fact, on metals with significant carbon solubility such as nickel, the formation of heterogeneous graphene with monolayer, bilayer, and few-layer is very common because of the additional graphene growth from the carbon reservoir in the catalyst bulk. Nevertheless, this segregation effect seems to be limited when 50 nm thick nickel is used compared with 25 nm thick nickel thin film, probably because a thicker Ni film (50 nm) presents a "deeper" reservoir of carbon than a thinner Ni film (25 nm) even when similar heating treatment is used for the two films. This may explain why the synthesized graphene was thicker with the 25 nm nickel film and thinner with the 50 nm nickel film.

Nickel thickness (nm)	Processing conditions	a-C thickness (nm)	Derived Graphene
25	900 °C with a heating rate of 15 °C/s, for 420 s and a cooling rate of 0.5 °C/s	2	Continuous uniform few-layer graphene
50			Continuous heterogeneous graphene with predominance of bilayer
150			Non-continuous heterogeneous graphene

Table 4: Summary of the different characteristics of the graphene resulting from the synthesis process using 25, 50, and 150 nm thick nickel film.

However, a further increase in nickel thickness up to 150 nm markedly affected the resulting graphene, which was non-continuous, even though monolayer, bilayer, and few-layer graphene with very low defect densities were observed. On one hand, this surface discontinuity may be due to the large attached nickel islands derived from the dewetting process of the 150 nm thick nickel film, or, on the other hand, to the low concentration of dissolved carbon that diffused deep into the thick nickel film. Because of the marked surface heterogeneity, it was not possible to perform the Raman statistical analysis to get an overview of the graphene layer distribution. From these results, we conclude that the larger amount of graphene is precipitated from the thinner nickel films whereas a smaller amount of graphene is precipitated from the thicker nickel films. Furthermore, as for the quality of graphene films, we can speculate that the increase in the number of layers is caused by the structural disorder of graphene films. This shows that the number of layers and the quality of the film (in terms of defects) can be controlled by choosing the appropriate thickness of the nickel for a given temperature.

In addition, let us recall that using 25, 50, and 150 nm thick Ni, the graphene not only forms on the surface of the nickel but also at the interface between the nickel and the SiO_2 substrate. This occurs because carbon diffuses through the nickel film during thermal annealing and segregates out of both sides of the Ni film, as illustrated in **Figure 9b**, which summarizes the mechanisms deduced from our experiments.

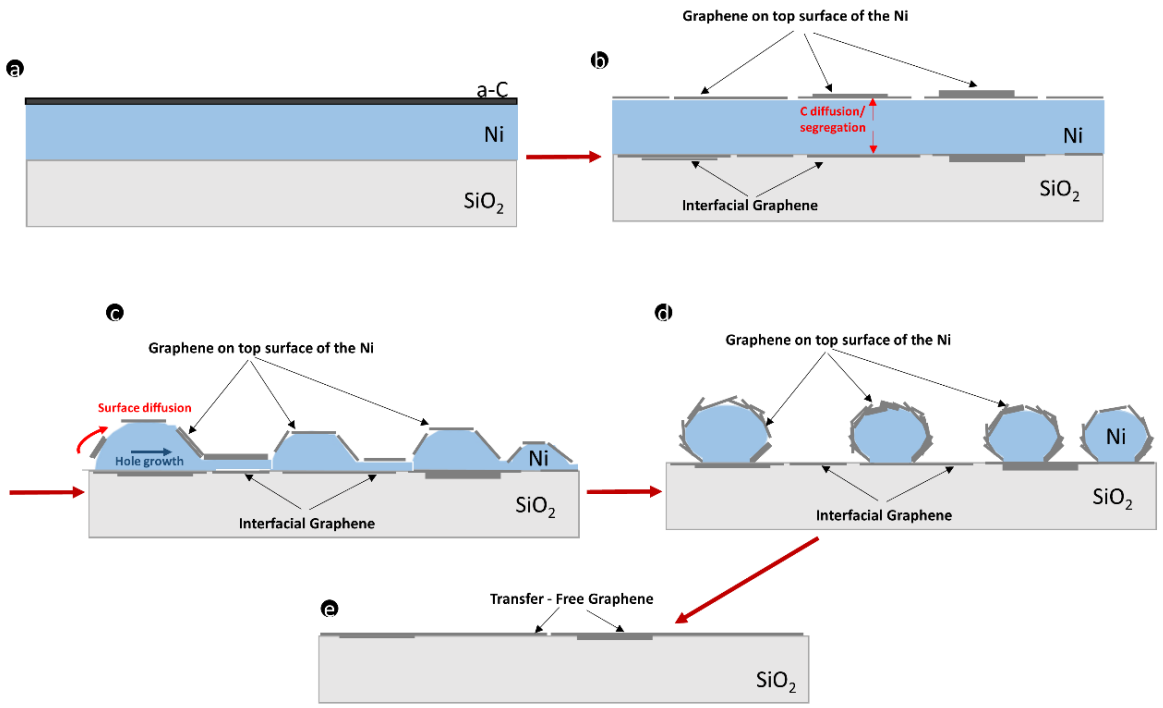

Figure 9: Schematic illustration of graphene growth on the surface of nickel film and in the interface between the Ni and SiO_2 substrate during the nickel dewetting process. (a) The initial stage of the a-C/Ni/SiO_2 before the rapid thermal annealing process. (b) The stage of carbon diffusion and segregation through the nickel leading to the initial formation of graphene before nickel dewetting begins. (c) The stage related to the beginning of the nickel dewetting. (d) The stage with the end of the nickel dewetting process. During stages (c) and (d), the initially formed graphene certainly undergoes further changes in nanostructure. (e) Interfacial graphene obtained with the thinnest Ni thicknesses (25-50 nm) after the removal of nickel particles with $FeCl_3$ treatment.

In our recent study **[25]**, using *in situ* XPS analysis, we demonstrated that graphene already forms at 500 °C through carbon diffusion and segregation in the nickel catalyst during the annealing process. A similar mechanism also occurs with thermal annealing up to 900 °C, but the highest temperatures also induce nickel dewetting, as we observed here. More precisely, as described in Fig.9, three main phenomena occur when the temperature is increased to 900 °C:

- At the lowest temperatures, typically 500 °C, carbon diffusion inside the Ni film (forming a Ni(C) film) and carbon segregation on both sides of the nickel film occur, forming defective graphene both on the surface of the Ni(C) film and at the interface between the Ni(C) film and the substrate, as shown in **Fig. 9b**. This explanation is based on the results of our previous work **[25]**, which showed graphene formation after annealing at 500 °C without Ni dewetting at this temperature.
- At higher temperatures (the exact values depend on the thickness of the Ni film), the dewetting of the Ni(C) film starts with the appearance of holes that grow in size, progressively leading to the formation of nickel islands, as depicted in **Fig. 9c**. This phenomenon does not prevent the graphene growth process producing less defective graphene present both around the nickel islands and on the surface of the substrate, despite retraction of the nickel film.
- At the highest temperatures, the final stage of the nickel dewetting transforms the nickel islands into individual particles (**Fig. 9d**) that are easily removed from the surface by chemical etching if the initial Ni film was sufficiently thin (25-50 nm). At this final stage, the surface of the SiO_2 substrate remains covered by large extents of graphene (**Fig. 9e**).

Deduced from our observations, this mechanism shows that the graphene synthesis is compatible with the nickel dewetting during thermal annealing. However, it depends to a great

extent on the initial thickness of the nickel film and on the annealing temperature. Indeed, using 25 and 50 nm thick nickel film, we observed the continuous surface and interfacial graphene growth with the formation of spherical nickel particles. When using 150 nm thick nickel, we observed non-continuous surface and growth of interfacial graphene with stringy nickel particles. In previous papers, Prekodravac et al. **[59, 60]** also observed the formation of graphene films with attention to the catalyst dewetting process during annealing. In one study **[59]**, a 200 nm thick carbon-doped nickel film was transformed into monolayer graphene islands among nickel grains, by RTA within 900-1000°C. In another study **[60]**, the authors used a bilayer Ni(50nm)/Cu(700 nm) deposited on polished polycrystalline graphite, annealed within 600-900°C for 30 mn, and at 900°C during longer periods. The lowest annealing temperatures led to discontinuous, high defective monolayer of graphene, whereas the highest temperatures led to homogeneous multilayer graphene with a lower defective content. In spite of a different configuration of metal catalyst, our investigations at 900°C confirm those previous works and widens the possibility to control the graphene growth concomitant with the catalyst dewetting in a similar way. Finally, after removal of the nickel islands with $FeCl_3$ treatment, we performed UV-Vis analysis on the continuous interfacial graphene obtained with the 25 and 50 nm thick nickel film, to quantify transmittance. **Fig. 10** shows measurement of transmittance of graphene derived from both 25 and 50 nm nickel after etching of nickel particles. The transmittance of the derived graphene from 25 nm nickel at 550 nm was ~84 %, which is consistent with values reported **[61–63]** for few-layer graphene (~3-6 layers). The transmittance value of the graphene resulting from 50 nm nickel was much higher, ~88%, which is consistent with the previously reported values **[31,64,65]** for bilayer graphene. Indeed, the transmittance of the synthetized graphene from 25 nm nickel was lower than the transmittance of graphene resulting from 50 nm thick nickel because it has more layers, as indicated by Raman data. These results are consistent with the principle that the optical transmittance is strongly correlated with the number of graphene layers. Graphene transmittance thus decreases with an increase in the number of layers **[66–68]**.

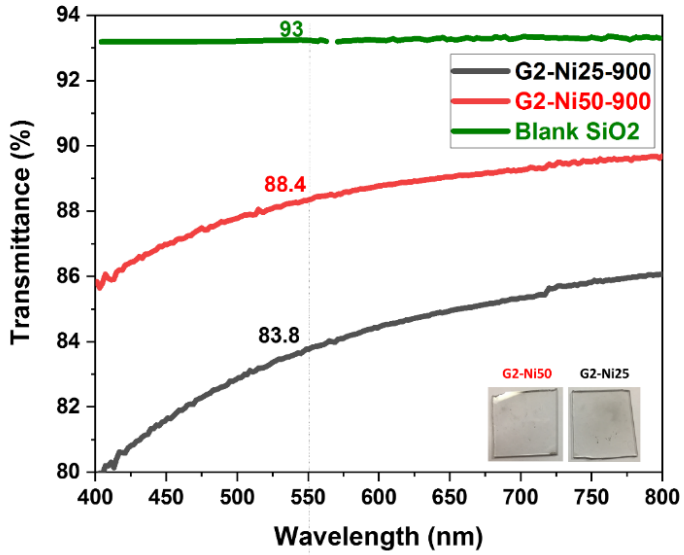

Figure 10: Transmittance curves as a function of wavelength for graphene derived from 25 nm thick nickel (bottom) and synthesized graphene derived from 50 nm thick nickel (middle) after thermal annealing and $FeCl_3$ etching and the blank fused silica (top). The inset at the bottom of the figure shows the appearance of both samples after graphene growth and Ni etching.

5. Conclusions

Here, we investigated the transformation of a thin amorphous carbon (a-C) film into transfer-free graphene using nickel catalyst dewetting phenomena. We conducted a systematic study of nickel dewetting, as well as of the effect of nickel thickness on graphene growth. The a-C layer was deposited on a Ni/SiO_2 substrate, followed by rapid thermal annealing. The annealing step caused the catalyst layer to fragment into stringy islands and particles, and graphene films formed on the surface of the nickel particles and at the interface between the nickel particles and the SiO_2 substrate. The most crucial parameters responsible for changes in the Ni film are annealing temperature, the thickness of the initial nickel film, and the thin carbon layer deposited on Ni prior to rapid thermal annealing that partially dissolved into Ni at high temperatures. Microscopic Raman mapping, SEM and HRTEM indicated that graphene films were preferentially continuous when 25 and 50 nm thick nickel was used, whereas the graphene synthetized from 150 nm thick nickel was discontinuous. We also confirmed that both the thickness of the graphene layer and the size of the nickel particles depend on the starting

thickness of the nickel. The synthesized graphene films had better structural qualities and fewer layers when the thickness of the nickel catalyst was increased from 25 to 50 nm. With acidic etching of the residual nickel, the substrate with graphene regained high transparency of about 88% corresponding to the bilayer interfacial graphene for the derived graphene from 50 nm of nickel. Our method thus extends the range of substrate materials on which graphene can be directly synthesized, thereby avoiding relatively complicated, costly and not always defect-free transfer techniques. We believe the present results provide useful information for a future graphene synthesis process using a catalytic reaction.

Acknowledgements

This work was supported by the LABEX MANUTECH-SISE (ANR-10-LABX-0075) of *Université de Lyon*, as part of the program "*Investissements d'Avenir*" (ANR-11-IDEX-0007) operated by the French National Research Agency (ANR).

References

[1] A.K. Geim, K.S. Novoselov, The rise of graphene, Nature Materials. 6 (2007) 183–191. https://doi.org/10.1038/nmat1849.

[2] K.S. Novoselov, A.K. Geim, S.V. Morozov, D. Jiang, Y. Zhang, S.V. Dubonos, I.V. Grigorieva, A.A. Firsov, Electric Field Effect in Atomically Thin Carbon Films, Science. 306 (2004) 666–669. https://doi.org/10.1126/science.1102896.

[3] R.R. Nair, P. Blake, A.N. Grigorenko, K.S. Novoselov, T.J. Booth, T. Stauber, N.M.R. Peres, A.K. Geim, Fine Structure Constant Defines Visual Transparency of Graphene, Science. 320 (2008) 1308–1308. https://doi.org/10.1126/science.1156965.

[4] Y.D. Kim, M.-H. Bae, J.-T. Seo, Y.S. Kim, H. Kim, J.H. Lee, J.R. Ahn, S.W. Lee, S.-H. Chun, Y.D. Park, Focused-Laser-Enabled p–n Junctions in Graphene Field-Effect Transistors, ACS Nano. 7 (2013) 5850–5857. https://doi.org/10.1021/nn402354j.

[5] F. Bonaccorso, Z. Sun, T. Hasan, A.C. Ferrari, Graphene photonics and optoelectronics, Nature Photonics. 4 (2010) 611–622. https://doi.org/10.1038/nphoton.2010.186.

[6] K.V. Emtsev, A. Bostwick, K. Horn, J. Jobst, G.L. Kellogg, L. Ley, J.L. McChesney, T. Ohta, S.A. Reshanov, J. Röhrl, E. Rotenberg, A.K. Schmid, D. Waldmann, H.B. Weber, T. Seyller, Towards wafer-size graphene layers by atmospheric pressure graphitization of silicon carbide, Nature Materials. 8 (2009) 203–207. https://doi.org/10.1038/nmat2382.

[7] X. Li, C.W. Magnuson, A. Venugopal, J. An, J.W. Suk, B. Han, M. Borysiak, W. Cai, A. Velamakanni, Y. Zhu, L. Fu, E.M. Vogel, E. Voelkl, L. Colombo, R.S. Ruoff, Graphene Films with Large Domain Size by a Two-Step Chemical Vapor Deposition Process, Nano Lett. 10 (2010) 4328–4334. https://doi.org/10.1021/nl101629g.

[8] R. Hawaldar, P. Merino, M.R. Correia, I. Bdikin, J. Grácio, J. Méndez, J.A. Martín-Gago, M.K. Singh, Large-area high-throughput synthesis of monolayer graphene sheet by Hot Filament Thermal Chemical Vapor Deposition, Scientific Reports. 2 (2012) 682. https://doi.org/10.1038/srep00682.

[9] S. Pei, H.-M. Cheng, The reduction of graphene oxide, Carbon. 50 (2012) 3210–3228. https://doi.org/10.1016/j.carbon.2011.11.010.
[10] Y. Bleu, F. Bourquard, T. Tite, A.-S. Loir, C. Maddi, C. Donnet, F. Garrelie, Review of Graphene Growth From a Solid Carbon Source by Pulsed Laser Deposition (PLD), Front Chem. 6 (2018). https://doi.org/10.3389/fchem.2018.00572.
[11] A. Reina, S. Thiele, X. Jia, S. Bhaviripudi, M.S. Dresselhaus, J.A. Schaefer, J. Kong, Growth of large-area single- and Bi-layer graphene by controlled carbon precipitation on polycrystalline Ni surfaces, Nano Research. 2 (2009) 509–516. https://doi.org/10.1007/s12274-009-9059-y.
[12] A. Delamoreanu, C. Rabot, C. Vallee, A. Zenasni, Wafer scale catalytic growth of graphene on nickel by solid carbon source, Carbon. 66 (2014) 48–56. https://doi.org/10.1016/j.carbon.2013.08.037.
[13] A.E.M. Abd Elhamid, M.A. Hafez, A.M. Aboulfotouh, I.M. Azzouz, Study of graphene growth on copper foil by pulsed laser deposition at reduced temperature, Journal of Applied Physics. 121 (2017) 025303. https://doi.org/10.1063/1.4973736.
[14] U. Narula, C.M. Tan, C.S. Lai, Copper induced synthesis of graphene using amorphous carbon, Microelectronics Reliability. 61 (2016) 87–90. https://doi.org/10.1016/j.microrel.2016.01.005.
[15] P. Tyagi, Z.R. Robinson, A. Munson, C.W. Magnuson, S. Chen, J.D. McNeilan, R.L. Moore, R.D. Piner, R.S. Ruoff, C.A. Ventrice, Characterization of graphene films grown on CuNi foil substrates, Surface Science. 634 (2015) 16–24. https://doi.org/10.1016/j.susc.2014.11.019.
[16] C.M. Orofeo, H. Ago, B. Hu, M. Tsuji, Synthesis of large area, homogeneous, single layer graphene films by annealing amorphous carbon on Co and Ni, Nano Research. 4 (2011) 531–540. https://doi.org/10.1007/s12274-011-0109-x.
[17] T. Tite, C. Donnet, A.-S. Loir, S. Reynaud, J.-Y. Michalon, F. Vocanson, F. Garrelie, Graphene-based textured surface by pulsed laser deposition as a robust platform for surface enhanced Raman scattering applications, Applied Physics Letters. 104 (2014) 041912.
[18] P. Fortgang, T. Tite, V. Barnier, N. Zehani, C. Maddi, F. Lagarde, A.-S. Loir, N. Jaffrezic-Renault, C. Donnet, F. Garrelie, C. Chaix, Robust Electrografting on Self-Organized 3D Graphene Electrodes, ACS Applied Materials & Interfaces. 8 (2016) 1424–1433. https://doi.org/10.1021/acsami.5b10647.
[19] C. Maddi, F. Bourquard, V. Barnier, J. Avila, M.-C. Asensio, T. Tite, C. Donnet, F. Garrelie, Nano-Architecture of nitrogen-doped graphene films synthesized from a solid CN source, Scientific Reports. 8 (2018). https://doi.org/10.1038/s41598-018-21639-9.
[20] A.T.T. Koh, Y.M. Foong, D.H.C. Chua, Comparison of the mechanism of low defect few-layer graphene fabricated on different metals by pulsed laser deposition, Diamond and Related Materials. 25 (2012) 98–102. https://doi.org/10.1016/j.diamond.2012.02.014.
[21] Y. Bleu, F. Bourquard, A.-S. Loir, V. Barnier, F. Garrelie, C. Donnet, Raman study of the substrate influence on graphene synthesis using a solid carbon source via rapid thermal annealing, Journal of Raman Spectroscopy. 50 (2019) 1630–1641. https://doi.org/10.1002/jrs.5683.
[22] H. Zhang, P.X. Feng, Fabrication and characterization of few-layer graphene, Carbon. 48 (2010) 359–364. https://doi.org/10.1016/j.carbon.2009.09.037.
[23] Y. Bleu, F. Bourquard, V. Barnier, Y. Lefkir, S. Reynaud, A.-S. Loir, F. Garrelie, C. Donnet, Boron-doped graphene synthesis by pulsed laser co-deposition of carbon and boron, Applied Surface Science. 513 (2020) 145843. https://doi.org/10.1016/j.apsusc.2020.145843.

[24] F. Bourquard, Y. Bleu, A.-S. Loir, B. Caja-Munoz, J. Avila, M.-C. Asensio, G. Raimondi, M. Shokouhi, I. Rassas, C. Farre, C. Chaix, V. Barnier, N. Jaffrezic-Renault, F. Garrelie, C. Donnet, Electroanalytical Performance of Nitrogen-Doped Graphene Films Processed in One Step by Pulsed Laser Deposition Directly Coupled with Thermal Annealing, Materials. 12 (2019) 666. https://doi.org/10.3390/ma12040666.
[25] Y. Bleu, V. Barnier, F. Christien, F. Bourquard, A.-S. Loir, F. Garrelie, C. Donnet, Dynamics of carbon diffusion and segregation through nickel catalyst, investigated by in-situ XPS, during the growth of nitrogen-doped graphene, Carbon. 155 (2019) 410–420. https://doi.org/10.1016/j.carbon.2019.08.084.
[26] M. Marchena, D. Janner, T.L. Chen, V. Finazzi, V. Pruneri, Low temperature direct growth of graphene patterns on flexible glass substrates catalysed by a sacrificial ultrathin Ni film, Opt. Mater. Express. 6 (2016) 2487. https://doi.org/10.1364/OME.6.002487.
[27] K. Nakagawa, H. Takahashi, Y. Shimura, H. Maki, A light emitter based on practicable and mass-producible polycrystalline graphene patterned directly on silicon substrates from a solid-state carbon source, RSC Adv. 9 (2019) 37906–37910. https://doi.org/10.1039/C9RA07294B.
[28] K. Banno, M. Mizuno, K. Fujita, T. Kubo, M. Miyoshi, T. Egawa, T. Soga, Transfer-free graphene synthesis on insulating substrates via agglomeration phenomena of catalytic nickel films, Appl. Phys. Lett. 103 (2013) 082112. https://doi.org/10.1063/1.4818342.
[29] A. Srivastava, C. Galande, L. Ci, L. Song, C. Rai, D. Jariwala, K.F. Kelly, P.M. Ajayan, Novel Liquid Precursor-Based Facile Synthesis of Large-Area Continuous, Single, and Few-Layer Graphene Films, Chem. Mater. 22 (2010) 3457–3461. https://doi.org/10.1021/cm101027c.
[30] K. Xu, P. Cao, J.R. Heath, Scanning Tunneling Microscopy Characterization of the Electrical Properties of Wrinkles in Exfoliated Graphene Monolayers, Nano Lett. 9 (2009) 4446–4451. https://doi.org/10.1021/nl902729p.
[31] Y. Bleu, F. Bourquard, V. Gartiser, A.-S. Loir, B. Caja-Munoz, J. Avila, V. Barnier, F. Garrelie, C. Donnet, Graphene synthesis on SiO2 using pulsed laser deposition with bilayer predominance, Materials Chemistry and Physics. 238 (2019) 121905. https://doi.org/10.1016/j.matchemphys.2019.121905.
[32] C.V. Thompson, Solid-State Dewetting of Thin Films, Annu. Rev. Mater. Res. 42 (2012) 399–434. https://doi.org/10.1146/annurev-matsci-070511-155048.
[33] H. Krishna, N. Shirato, C. Favazza, R. Kalyanaraman, Energy driven self-organization in nanoscale metallic liquid films, Phys. Chem. Chem. Phys. 11 (2009) 8136–8143. https://doi.org/10.1039/B906281P.
[34] J.-Y. Kwon, T.-S. Yoon, K.-B. Kim, S.-H. Min, Comparison of the agglomeration behavior of Au and Cu films sputter deposited on silicon dioxide, Journal of Applied Physics. 93 (2003) 3270–3278. https://doi.org/10.1063/1.1556178.
[35] F. Ruffino, M. Censabella, M.G. Grimaldi, Dewetted Pt nanostructures on Silicon Carbide surface, Journal of Physics and Chemistry of Solids. 140 (2020) 109403. https://doi.org/10.1016/j.jpcs.2020.109403.
[36] S.J. Henley, J.D. Carey, S.R.P. Silva, Pulsed-laser-induced nanoscale island formation in thin metal-on-oxide films, Phys. Rev. B. 72 (2005) 195408. https://doi.org/10.1103/PhysRevB.72.195408.
[37] A. Geissler, M. He, J.-M. Benoit, P. Petit, Effect of Hydrogen Pressure on the Size of Nickel Nanoparticles Formed during Dewetting and Reduction of Thin Nickel Films, J. Phys. Chem. C. 114 (2010) 89–92. https://doi.org/10.1021/jp908427r.
[38] M. Chhowalla, K.B.K. Teo, C. Ducati, N.L. Rupesinghe, G.A.J. Amaratunga, A.C. Ferrari, D. Roy, J. Robertson, W.I. Milne, Growth process conditions of vertically

aligned carbon nanotubes using plasma enhanced chemical vapor deposition, Journal of Applied Physics. 90 (2001) 5308–5317. https://doi.org/10.1063/1.1410322.
[39] S. Elnobi, S. Sharma, M. Ibrahim Araby, B. Paudel, G. Kalita, M.Z.M. Yusop, M. Emre Ayhan, M. Tanemura, Room-temperature graphitization in a solid-phase reaction, RSC Advances. 10 (2020) 914–922. https://doi.org/10.1039/C9RA09038J.
[40] A.C. Ferrari, J.C. Meyer, V. Scardaci, C. Casiraghi, M. Lazzeri, F. Mauri, S. Piscanec, D. Jiang, K.S. Novoselov, S. Roth, A.K. Geim, Raman Spectrum of Graphene and Graphene Layers, Phys. Rev. Lett. 97 (2006) 187401. https://doi.org/10.1103/PhysRevLett.97.187401.
[41] D. Graf, F. Molitor, K. Ensslin, C. Stampfer, A. Jungen, C. Hierold, L. Wirtz, Raman mapping of a single-layer to double-layer graphene transition, Eur. Phys. J. Spec. Top. 148 (2007) 171–176. https://doi.org/10.1140/epjst/e2007-00237-1.
[42] L.M. Malard, M.A. Pimenta, G. Dresselhaus, M.S. Dresselhaus, Raman spectroscopy in graphene, Physics Reports. 473 (2009) 51–87. https://doi.org/10.1016/j.physrep.2009.02.003.
[43] Y. Gong, X. Zhang, G. Liu, L. Wu, X. Geng, M. Long, X. Cao, Y. Guo, W. Li, J. Xu, M. Sun, L. Lu, L. Liu, Layer-Controlled and Wafer-Scale Synthesis of Uniform and High-Quality Graphene Films on a Polycrystalline Nickel Catalyst, Advanced Functional Materials. 22 (2012) 3153–3159. https://doi.org/10.1002/adfm.201200388.
[44] W. Xiong, Y.S. Zhou, L.J. Jiang, A. Sarkar, M. Mahjouri-Samani, Z.Q. Xie, Y. Gao, N.J. Ianno, L. Jiang, Y.F. Lu, Single-Step Formation of Graphene on Dielectric Surfaces, Advanced Materials. 25 (2013) 630–634. https://doi.org/10.1002/adma.201202840.
[45] Z. Peng, Z. Yan, Z. Sun, J.M. Tour, Direct Growth of Bilayer Graphene on SiO2 Substrates by Carbon Diffusion through Nickel, ACS Nano. 5 (2011) 8241–8247. https://doi.org/10.1021/nn202923y.
[46] L.G. Cançado, K. Takai, T. Enoki, M. Endo, Y.A. Kim, H. Mizusaki, A. Jorio, L.N. Coelho, R. Magalhães-Paniago, M.A. Pimenta, General equation for the determination of the crystallite size La of nanographite by Raman spectroscopy, Appl. Phys. Lett. 88 (2006) 163106. https://doi.org/10.1063/1.2196057.
[47] G. Kalita, K. Wakita, M. Umeno, Monolayer graphene from a green solid precursor, Physica E: Low-Dimensional Systems and Nanostructures. 43 (2011) 1490–1493. https://doi.org/10.1016/j.physe.2011.04.014.
[48] S. Sharma, G. Kalita, R. Hirano, Y. Hayashi, M. Tanemura, Influence of gas composition on the formation of graphene domain synthesized from camphor, Materials Letters. 93 (2013) 258–262. https://doi.org/10.1016/j.matlet.2012.11.090.
[49] M.-H. Park, T.-H. Kim, C.-W. Yang, Thickness contrast of few-layered graphene in SEM, Surface and Interface Analysis. 44 (2012) 1538–1541. https://doi.org/10.1002/sia.4995.
[50] Y. Zhou, D.S. Fox, P. Maguire, R. O'Connell, R. Masters, C. Rodenburg, H. Wu, M. Dapor, Y. Chen, H. Zhang, Quantitative secondary electron imaging for work function extraction at atomic level and layer identification of graphene, Sci Rep. 6 (2016) 1–8. https://doi.org/10.1038/srep21045.
[51] H. Hiura, H. Miyazaki, K. Tsukagoshi, Determination of the Number of Graphene Layers: Discrete Distribution of the Secondary Electron Intensity Stemming from Individual Graphene Layers, Appl. Phys. Express. 3 (2010) 095101. https://doi.org/10.1143/APEX.3.095101.
[52] J.D. Carey, L.L. Ong, S.R.P. Silva, Formation of low-temperature self-organized nanoscale nickel metal islands, Nanotechnology. 14 (2003) 1223–1227. https://doi.org/10.1088/0957-4484/14/11/011.

[53] K. Mougin, Z. Zheng, N. Piazzon, E. Gnecco, H. Haidara, Thermal stability and reconstruction of nanoparticulate Au film on model molecular surfaces, Journal of Colloid and Interface Science. 333 (2009) 719–724. https://doi.org/10.1016/j.jcis.2009.01.044.
[54] R. Nuryadi, Y. Ishikawa, Y. Ono, M. Tabe, Thermal agglomeration of single-crystalline Si layer on buried SiO2 in ultrahigh vacuum, Journal of Vacuum Science & Technology B: Microelectronics and Nanometer Structures Processing, Measurement, and Phenomena. 20 (2002) 167–172. https://doi.org/10.1116/1.1431956.
[55] Sudheer, P. Mondal, V.N. Rai, A.K. Srivastava, A study of growth and thermal dewetting behavior of ultra-thin gold films using transmission electron microscopy, AIP Advances. 7 (2017) 075303. https://doi.org/10.1063/1.4989823.
[56] M. Diarra, A. Zappelli, H. Amara, F. Ducastelle, C. Bichara, Importance of Carbon Solubility and Wetting Properties of Nickel Nanoparticles for Single Wall Nanotube Growth, Phys. Rev. Lett. 109 (2012) 185501. https://doi.org/10.1103/PhysRevLett.109.185501.
[57] M. Miyoshi, M. Mizuno, K. Banno, T. Kubo, T. Egawa, T. Soga, Study on transfer-free graphene synthesis process utilizing spontaneous agglomeration of catalytic Ni and Co metals, Mater. Res. Express. 2 (2015) 015602. https://doi.org/10.1088/2053-1591/2/1/015602.
[58] E. Kim, W.-G. Lee, J. Jung, Agglomeration effects of thin metal catalyst on graphene film synthesized by chemical vapor deposition, Electron. Mater. Lett. 7 (2011) 261–264. https://doi.org/10.1007/s13391-011-0915-z.
[59] J.R. Prekodravac, S.P. Jovanović, I.D. Holclajtner-Antunović, D.B. Peruško, V.B. Pavlović, D.D. Tošić, B.M. Todorović-Marković, Z.M. Marković, Monolayer graphene films through nickel catalyzed transformation of fullerol and graphene quantum dots: a Raman spectroscopy study, Phys. Scr. 2014 (2014) 014030. https://doi.org/10.1088/0031-8949/2014/T162/014030.
[60] J. Prekodravac, Z. Marković, S. Jovanović, M. Budimir, D. Peruško, I. Holclajtner-Antunović, V. Pavlović, Z. Syrgiannis, A. Bonasera, B. Todorović-Marković, The effect of annealing temperature and time on synthesis of graphene thin films by rapid thermal annealing, Synthetic Metals. 209 (2015) 461–467. https://doi.org/10.1016/j.synthmet.2015.08.015.
[61] H.J. Park, J. Meyer, S. Roth, V. Skákalová, Growth and properties of few-layer graphene prepared by chemical vapor deposition, Carbon. 48 (2010) 1088–1094. https://doi.org/10.1016/j.carbon.2009.11.030.
[62] X. Fan, T. Chen, L. Dai, Graphene networks for high-performance flexible and transparent supercapacitors, RSC Adv. 4 (2014) 36996–37002. https://doi.org/10.1039/C4RA05076B.
[63] Y.-Z. Chen, H. Medina, H.-C. Lin, H.-W. Tsai, T.-Y. Su, Y.-L. Chueh, Large-scale and patternable graphene: direct transformation of amorphous carbon film into graphene/graphite on insulators via Cu mediation engineering and its application to all-carbon based devices, Nanoscale. 7 (2015) 1678–1687. https://doi.org/10.1039/C4NR04627G.
[64] S. Lee, K. Lee, C.-H. Liu, Z. Zhong, Homogeneous bilayer graphene film based flexible transparent conductor, Nanoscale. 4 (2012) 639–644. https://doi.org/10.1039/C1NR11574J.
[65] H.A. Chaliyawala, N. Rajaram, R. Patel, A. Ray, I. Mukhopadhyay, Controlled Island Formation of Large-Area Graphene Sheets by Atmospheric Chemical Vapor Deposition: Role of Natural Camphor, ACS Omega. 4 (2019) 8758–8766. https://doi.org/10.1021/acsomega.9b00051.

[66] T. Lin, F. Huang, D. Wan, H. Bi, X. Xie, M. Jiang, Self-regulating homogenous growth of high-quality graphene on Co–Cu composite substrate for layer control, Nanoscale. 5 (2013) 5847–5853. https://doi.org/10.1039/C3NR33124E.
[67] Z. Tu, Z. Liu, Y. Li, F. Yang, L. Zhang, Z. Zhao, C. Xu, S. Wu, H. Liu, H. Yang, P. Richard, Controllable growth of 1–7 layers of graphene by chemical vapour deposition, Carbon. 73 (2014) 252–258. https://doi.org/10.1016/j.carbon.2014.02.061.
[68] K.-J. Peng, C.-L. Wu, Y.-H. Lin, Y.-J. Liu, D.-P. Tsai, Y.-H. Pai, G.-R. Lin, Hydrogen-free PECVD growth of few-layer graphene on an ultra-thin nickel film at the threshold dissolution temperature, J. Mater. Chem. C. 1 (2013) 3862–3870. https://doi.org/10.1039/C3TC30332B.

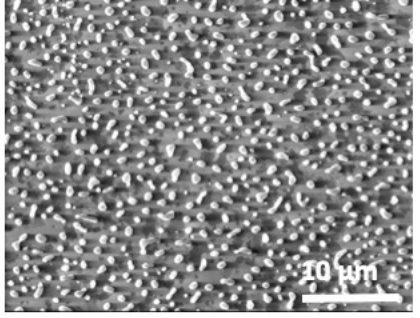
10 µm

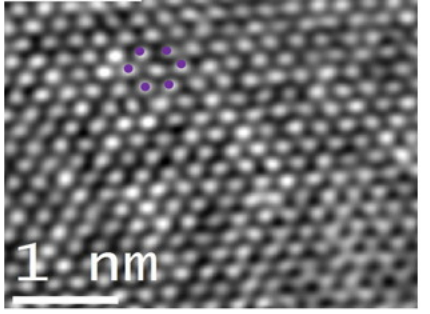
1 nm

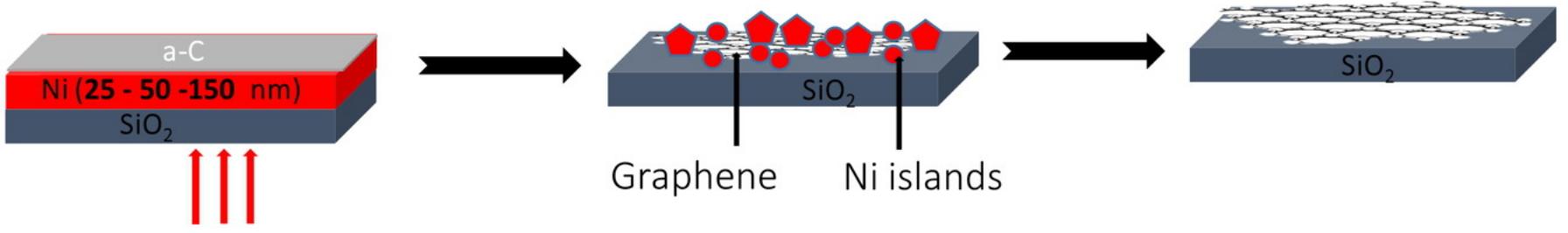
a-C
Ni (25 - 50 -150 nm)
SiO2
Heating 900°C in vacuum
SiO2
Graphene
Ni islands
SiO2